

JGR Solid Earth

RESEARCH ARTICLE

10.1029/2022JB026165

Key Points:

- We studied rheology of hexagonal close-packed Fe based on high-pressure and high-temperature deformation experiments
- Dominant deformation mechanism was power-law dislocation creep at temperatures above ~ 800 K
- We estimated the viscosity of hexagonal close-packed Fe under inner core conditions as $\geq \sim 10^{19}$ Pa s

Supporting Information:

Supporting Information may be found in the online version of this article.

Correspondence to:

Y. Nishihara,
yunishi@sci.ehime-u.ac.jp

Citation:

Nishihara, Y., Doi, S., Tsujino, N., Yamazaki, D., Matsukage, K. N., Tsubokawa, Y., et al. (2023). Rheology of hexagonal close-packed (hcp) iron. *Journal of Geophysical Research: Solid Earth*, 128, e2022JB026165. <https://doi.org/10.1029/2022JB026165>

Received 1 DEC 2022

Accepted 21 MAY 2023

Author Contributions:

Conceptualization: Yu Nishihara
Funding acquisition: Yu Nishihara
Investigation: Yu Nishihara, Shunta Doi, Noriyoshi Tsujino, Daisuke Yamazaki, Kyoko N. Matsukage, Yumiko Tsubokawa, Takashi Yoshino, Andrew R. Thomson
Methodology: Yu Nishihara, Shunta Doi, Noriyoshi Tsujino, Daisuke Yamazaki
Project Administration: Yu Nishihara
Resources: Yuji Higo, Yoshinori Tange
Writing – original draft: Yu Nishihara

© 2023. The Authors.

This is an open access article under the terms of the Creative Commons Attribution License, which permits use, distribution and reproduction in any medium, provided the original work is properly cited.

Rheology of Hexagonal Close-Packed (hcp) Iron

Yu Nishihara¹ , Shunta Doi¹ , Noriyoshi Tsujino^{2,3} , Daisuke Yamazaki², Kyoko N. Matsukage⁴, Yumiko Tsubokawa^{1,5}, Takashi Yoshino² , Andrew R. Thomson⁶ , Yuji Higo³ , and Yoshinori Tange³

¹Geodynamics Research Center, Ehime University, Matsuyama, Japan, ²Institute of Planetary Materials, Okayama University, Misasa, Japan, ³Japan Synchrotron Radiation Research Institute, Sayo-gun, Japan, ⁴Department of Natural and Environmental Science, Teikyo University of Science, Adachi-ku, Tokyo, Japan, ⁵Department of Earth and Planetary Sciences, Kyushu University, Fukuoka, Japan, ⁶Department of Earth Sciences, University College London, London, UK

Abstract The viscosity of hexagonal close-packed (hcp) Fe is a fundamental property controlling the dynamics of the Earth's inner core. We studied the rheology of hcp-Fe using high-pressure and -temperature deformation experiments with in situ stress and strain measurements. Experiments were conducted using D111-type and deformation-DIA apparatuses at pressures of 16.3–22.6 GPa, temperatures of 423–923 K, and uniaxial strain rates of 1.52×10^{-6} to 8.81×10^{-5} s $^{-1}$ in conjunction with synchrotron radiation. Experimental results showed that power-law dislocation creep with a stress exponent of $n = 4.0 \pm 0.3$, activation energy of $E^* = 240 \pm 20$ kJ/mol, and activation volume of $V^* = 1.4 \pm 0.2$ cm 3 /mol is dominant deformation mechanism at $> \sim 800$ K, whereas a mechanism with power-law breakdown prevails at lower temperatures. An extrapolation of the power-law dislocation creep flow law based on homologous temperature scaling suggests the viscosity of hcp-Fe under inner core conditions is $\geq \sim 10^{19}$ Pa s. If this power-law dislocation creep mechanism is assumed to be the dominant mechanism in the Earth's inner core, the equatorial growth or translation mode mechanism may be the dominant geodynamical mechanism causing the observed inner core structure.

Plain Language Summary Although many geodynamic mechanisms have been proposed regarding the origin of the observed complex structure of Earth's inner core, no clear consensus has been reached. This is partly owing to the lack of accurate knowledge of the viscosity in the inner core, which is believed to mostly comprise of hexagonal close-packed Fe (hcp-Fe). Here, we studied the viscosity of hcp-Fe using high-pressure and high-temperature deformation experiments. The results showed that the dominant deformation mechanism in hcp-Fe changes depending on the temperature, with power-law dislocation creep and low-temperature creep being most important above and below ~ 800 K, respectively. Based on extrapolation of these experimental results we estimate the inner core viscosity to be $\geq 10^{19}$ Pa s. This inner core viscosity suggests the equatorial growth or translation mode model as the dominant geodynamical mechanism in the Earth's inner core.

1. Introduction

Seismic studies have revealed the existence of anisotropic and heterogeneous structures throughout the Earth's inner core (e.g., Brett & Deuss, 2020; Frost et al., 2021; Morelli et al., 1986; Wang et al., 2015; Woodhouse et al., 1986). The single most notable structure of the inner core is that compressional waves travel $\sim 3\%$ faster in north-south directions, compared with those in the equatorial plane (e.g., Creager, 1992). Recent studies have further clarified the details of the inner core's structure with (a) anisotropy observed to be stronger in the western hemisphere, (b) the central portion's anisotropy being tilted from polar direction, and (c) the outermost 50–150 km being nearly isotropic. Although several geodynamic mechanisms have been proposed for the origin of these observed inner core structures, a clear consensus is still to be reached (e.g., Lasbleis & Deguen, 2015; Romanowicz et al., 2016; Sumita & Bergman, 2007).

The viscosity of the inner core is one of the most important parameters in determining the dominant geodynamic mechanisms occurring within the inner core. Lasbleis and Deguen (2015) developed regime diagrams for inner core dynamics, describing dominant mechanisms as a function of control parameters. According to their analysis, in the case of unstable stratification, translation mode (global translation of the inner core with solidification on one hemisphere and melting on the other) (Monnereau et al., 2010) and plume convection (Jeanloz & Wenk, 1988) are predicted to be the dominant mechanisms when the inner core viscosity is above and below $\sim 10^{18}$ Pa s, respectively. In the case of stable stratification, equatorial inner core growth (deformation of inner

core due to preferential growth in equatorial belt) (Yoshida et al., 1996) and tangential Lorenz force (Buffett & Wenk, 2001) are regarded as the dominant mechanisms when the inner core viscosity is above and below $\sim 10^{12}$ Pa s, respectively. An accurate understanding of the inner core viscosity is needed for a more accurate constraint of the inner core dynamics.

The Earth's core is primarily composed of Fe with lesser amounts of Ni and light elements (possible candidates are Si, S, H, O, and C) (e.g., Alfè et al., 2002; Badro et al., 2014; Birch, 1952; Hirose et al., 2021; Sata et al., 2010). Although the crystal structure of Fe at conditions of the inner core is considered to be hexagonal close-packed (hcp) structure (e.g., Tateno et al., 2010), the viscosity of the inner core has been estimated mostly based on the experimentally determined diffusion coefficient of face-centered cubic (fcc) Fe owing to the technical difficulties of performing diffusion experiments at pressure and temperature in the hcp-Fe stability condition. The estimated viscosity values at the inner core conditions differ between published studies with estimates of 10^{20-22} Pa s (Reaman et al., 2012), or $\sim 10^{22-25}$ Pa s (Tsujino et al., 2020) for dislocation creep. Ritterbex and Tsuchiya (2020) estimated the inner core viscosity as $\sim 10^{17\pm 1}$ Pa s in the dislocation creep regime based on the self-diffusion coefficient of hcp-Fe, which they calculated using density functional theory. The variation in the estimated viscosity values is partly owing to the differences in the assumed parameters (e.g., stress exponent) used to calculate viscosity using the diffusion coefficient. An experimental study in which the viscosity of hcp-Fe is directly determined from analyses of deformation experiments would provide valuable insight into the viscosity of the inner core.

Although there are number of deformation studies on hcp-Fe, most of them are focused on texture development and operating slip systems (Merkel et al., 2004, 2012; Miyagi et al., 2008; Nishihara et al., 2018; Wenk et al., 2000). On the other hand, only a limited number of experimental studies on the rheology (viscosity) of hcp-Fe have been reported. Nishiyama et al. (2007) conducted deformation experiments on hcp-Fe using a deformation-DIA apparatus (D-DIA) at a pressure (P) of 16–18 GPa and a temperature (T) of 300–600 K, and reported a stress–strain rate relationship fitted to their observations. Gleason and Mao (2013) measured deviatoric stress observed in uniaxially compressed hcp-Fe in a diamond-anvil cell up to $P = 200$ GPa at room temperature. Because the experimental conditions were limited to relatively low temperatures, the deformation mechanism in these studies likely differs from that occurring in the inner core, where the temperature is close to the melting temperature. This leads to a large uncertainty in the understanding of the viscosity of hcp-Fe in the inner core. Deformation experiments on hcp-Fe at higher temperatures are needed.

In this study, the rheology of hcp-Fe was investigated by high-pressure and high-temperature deformation experiments. Uniaxial deformation experiments were conducted on hcp-Fe samples using D111-type and D-DIA apparatuses at $P = 16.3$ – 22.6 GPa, $T = 423$ – 923 K, and a uniaxial strain rate of 1.52×10^{-6} to 8.81×10^{-5} s $^{-1}$ with the stress–strain rate relationships monitored throughout in situ during deformation. Based on these results we constrain a flow law of hcp-Fe and use it to constrain and discuss the viscosity in Earth's inner core.

2. Experimental Procedures

2.1. Sample Preparation

Presintered polycrystalline iron aggregates were used in deformation experiments, which were sintered by hot-pressing reagent grade Fe sponge (99.9% purity, Wako Pure Chemical Industries) at ~ 1 GPa and 873 K in a Kawai-type multi-anvil press installed at the Geodynamics Research Center, Ehime University. The sintering conditions were within stability field of the body-centered cubic (bcc) structure of metallic iron, which can be recovered to ambient conditions. The materials used in the experiment were similar to those used in a previous study (Nishihara et al., 2018) and are known to contain small amounts (<1%) of iron oxide, most likely wüstite (FeO), which had formed on the surface of the grains in the starting material (see Figure 1a of Nishihara et al., 2018). The original grain size of bcc-Fe was estimated to be a few micro-meters based on the distribution of the iron oxide particles. The sintered polycrystalline iron samples were shaped into cylinders with a diameter of ~ 0.55 mm and a length of 0.5 mm for use in subsequent deformation experiments.

2.2. Deformation Experiments

We performed most of the high- P deformation experiments with a D111-type apparatus, which is a larger version of the deformation T-Cup (Hunt et al., 2014). Some additional experiments (M2190, 2606, and 2609) utilized a D-DIA apparatus. Experimental setups for each system are described below.

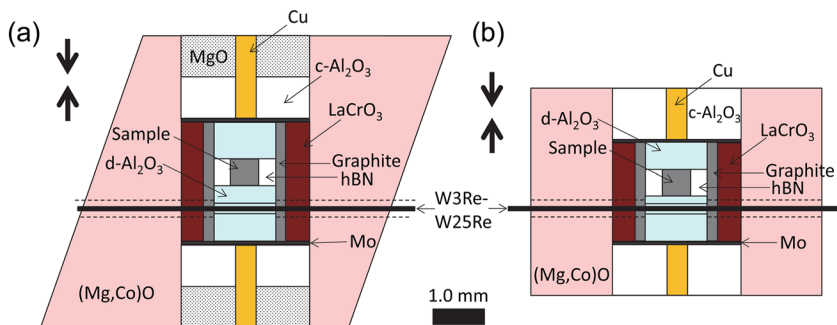


Figure 1. Schematic illustrations of (a) 7M/2 assembly used in deformation experiments with D111-type apparatus and (b) 4M/2.5 assembly used in deformation experiments with D-DIA apparatus. The c- and d-Al₂O₃ are crushable- and dense-Al₂O₃, respectively. The X-ray passed through perpendicular to page.

D111 experiments were performed at synchrotron beamline NE7A at PF-AR, KEK, Tsukuba, Japan (Nishihara, Tsujino, et al., 2020; Thomson et al., 2023; Tsujino et al., 2022). Throughout D111 experiments, 7M/2 assemblies were employed, denoting the (Mg,Co)O octahedral pressure medium with 7 mm edge lengths and anvils with 2 mm truncation edge lengths. In each experiment, pressure was generated using six tungsten carbide anvils combined with two anvils made from either cubic boron nitride (cBN) or diamond (with a SiC binder). These latter anvils are essential to allow collection of azimuthal diffraction rings of the sample, which are used to determine lattice strain, and subsequently stress, throughout deformation. The cell assembly (Figure 1a) used throughout experiments consists of a cylindrical graphite heater with LaCrO₃ thermal insulator. Samples were packed in hexagonal boron nitride (hBN) sleeves and sandwiched between dense Al₂O₃ pistons. In some runs, a 10 µm thick Au foil was placed at either ends of sample to increase the clarity of the sample ends in X-ray radiography. Temperatures were monitored using a W3%Re-W25%Re thermocouples placed adjacent to the sample. The (Mg,Co)O octahedron and the LaCrO₃ sleeve along the X-ray beam path were replaced with amorphous boron epoxy (in a ratio by weight of 20:1) and hBN, respectively, to minimize X-ray absorption and diffraction from these materials. Figure S1 in Supporting Information S1 shows the load–pressure relationship in the experiments with a D111-type apparatus using the 7M/2 assembly, with pressures up to 23 GPa achieved at press loads of 300 tf.

D-DIA experiments were performed using SPEED-MkII-D (Kawazoe et al., 2011) installed on the beamline BL04B1 at the SPring-8 synchrotron facility in Japan. In these runs, a cell assembly consisting of a (Mg,Co) O cubic pressure medium with 4 mm edge lengths and anvils with 2.5 mm truncation edge lengths were used (Figure 1b). Full details are provided in Nishihara et al. (2018).

All deformation experiments, both D111-type and D-DIA apparatuses were conducted in a similar manner. First, the cell assemblies were quasi-hydrostatically pressurized to the desired press load before heating to the target temperature. Before commencing uniaxial deformation, Fe samples were annealed at 723–923 K to ensure full stabilization of hcp-structure and the sample microstructure. Annealing times varied depending on the annealing temperature, such that durations were 90 min at 723 K, >40 min at 823–873 K, and 25 min at 923 K. Subsequently assemblies were uniaxially deformed by advancing the top and bottom anvils toward each other at a constant (and controlled) D-ram displacement rate. Temperatures were controlled to within ± 10 K of the nominal value during deformation, with one exception (M2190-2). A total of 12 experiments were conducted (Table 1). Each experiment consisted of several deformation steps at multiple conditions those within the range of 16.25–22.57 GPa, 423–923 K, and uniaxial strain rate ($\dot{\epsilon} = \partial\epsilon/\partial t$) of 1.52×10^{-6} to 8.81×10^{-5} s⁻¹. In *stepped strain rate tests*, we changed strain rate stepwise during one run at nearly constant P and T conditions. Similarly, in the *stepped temperature and pressure tests*, only the temperature or pressure were altered in a stepwise manner. After the completion of each series of deformation conditions, the power was shut off to temperature quench the experiment. Because the temperature reported in this paper is the nominal temperature measured at a slightly off-center part of the assembly, the average temperature of the specimens may have been higher by up to 10–50 K, since temperature gradients in high-pressure cell assemblies can be significant over sub-millimeter distances (Raterron et al., 2013). We ignored the effect of pressure on the temperature measurements using a W3%Re-W25%Re thermocouple because the estimated pressure effect is comparable to, or smaller than, the above temperature uncertainty (Nishihara, Doi, et al., 2020).

Table 1
Experimental Conditions and Results

Run number	Pressure (GPa)	Temperature (K)	Strain	Strain rate (10^{-5} s^{-1})	Stress (GPa)			
					$10\bar{1}0$	0002	$10\bar{1}1$	$10\bar{1}2$
<i>Stepped strain rate tests</i>								
Iron01	-1	17.36	823	0.011	0.15	0.49 ± 0.03	0.36 ± 0.02	0.37 ± 0.02
	-2	17.26	823	0.017	0.55	0.67 ± 0.03	0.55 ± 0.03	0.46 ± 0.02
Iron11	-1	22.57	823	0.017	0.37	0.58 ± 0.05	0.58 ± 0.05	0.52 ± 0.03
	-2	22.18	823	0.013	0.75	0.80 ± 0.05	0.79 ± 0.06	0.62 ± 0.03
Iron12	-1	17.29	823	0.024	0.41	1.09 ± 0.08	0.90 ± 0.07	0.72 ± 0.04
	-2	16.84	823	0.020	1.36	1.43 ± 0.08	1.14 ± 0.07	0.82 ± 0.04
	-3	16.49	823	0.031	5.09	1.51 ± 0.07	1.18 ± 0.06	0.86 ± 0.03
Iron26	-1	16.99	873	0.025	0.98	0.34 ± 0.03	0.28 ± 0.03	0.29 ± 0.02
	-2	17.05	873	0.016	0.57	0.32 ± 0.03	0.26 ± 0.03	0.27 ± 0.02
	-3	16.94	873	0.018	0.35	0.29 ± 0.03	0.24 ± 0.03	0.24 ± 0.02
	-4	16.83	873	0.040	1.82	0.49 ± 0.04	0.40 ± 0.04	0.38 ± 0.03
	-5	16.65	873	0.059	4.16	0.58 ± 0.05	0.47 ± 0.04	0.44 ± 0.04
M2190	-1	17.19	723	0.062	0.79	1.95 ± 0.03	1.42 ± 0.04	1.25 ± 0.03
	-2 ^a	16.96	723	0.093	4.14	2.05 ± 0.03	1.49 ± 0.04	1.33 ± 0.03
<i>Stepped temperature tests</i>								
Iron06	-1	17.21	823	0.032	0.57	0.68 ± 0.04	0.54 ± 0.04	0.50 ± 0.02
	-2	17.07	773	0.020	0.76	1.08 ± 0.04	0.93 ± 0.04	0.71 ± 0.02
	-3	16.87	723	0.023	0.90	1.38 ± 0.04	1.24 ± 0.05	0.87 ± 0.02
Iron13	-1	16.48	823	0.032	1.69	0.75 ± 0.03	0.61 ± 0.03	0.60 ± 0.04
	-2	16.50	773	0.034	2.26	1.19 ± 0.06	1.02 ± 0.05	0.79 ± 0.03
	-3	16.25	723	0.045	2.91	1.62 ± 0.07	1.36 ± 0.06	0.96 ± 0.03
Iron17	-1	20.62	923	0.014	0.89	-	-	-
	-2	20.26	873	0.029	1.42	0.47 ± 0.08	0.31 ± 0.07	0.33 ± 0.03
	-3	19.90	823	0.047	2.08	0.91 ± 0.09	0.72 ± 0.08	0.56 ± 0.03
M2606	-1	17.18	723	0.030	0.79	1.95 ± 0.02	1.59 ± 0.04	1.25 ± 0.03
	-2	17.44	623	0.018	0.75	2.69 ± 0.02	2.03 ± 0.09	1.70 ± 0.04
	-3	17.58	523	0.021	0.87	2.96 ± 0.03	2.34 ± 0.11	1.86 ± 0.05
	-4	17.74	423	0.027	1.09	2.96 ± 0.04	2.62 ± 0.12	1.87 ± 0.05
<i>Stepped pressure tests</i>								
Iron14	-1	16.56	823	0.039	1.31	0.99 ± 0.04	0.81 ± 0.04	0.65 ± 0.02
	-2	21.35	823	0.031	1.12	1.16 ± 0.04	1.09 ± 0.04	0.77 ± 0.02
<i>Others</i>								
Iron25	-1	17.50	823	0.031	0.92	0.66 ± 0.05	0.53 ± 0.03	0.50 ± 0.02
	-2	17.41	848	0.027	1.26	0.56 ± 0.05	0.44 ± 0.03	0.43 ± 0.02
	-3	17.13	873	0.028	1.52	0.46 ± 0.04	0.35 ± 0.03	0.35 ± 0.02
	-4	16.80	873	0.040	3.87	0.57 ± 0.05	0.43 ± 0.03	0.42 ± 0.02
	-5	16.50	873	0.056	8.81	0.69 ± 0.05	0.51 ± 0.04	0.48 ± 0.02
M2609	-1	16.92	623	0.023	0.51	2.70 ± 0.03	2.22 ± 0.07	1.68 ± 0.04
	-2	17.53	623	0.042	2.58	2.86 ± 0.03	1.98 ± 0.10	1.80 ± 0.05
								1.32 ± 0.02

Table 1
Continued

Run number	Pressure (GPa)	Temperature (K)	Strain (10^{-5} s^{-1})	Stress (GPa)			
				$10\bar{1}0$	0002	$10\bar{1}1$	$10\bar{1}2$
-3	17.62	523	0.035	0.69	3.07 ± 0.03	2.58 ± 0.09	1.95 ± 0.05
-4	17.56	523	0.054	3.04	2.87 ± 0.06	2.65 ± 0.08	1.81 ± 0.05

Note. Runs with series of run number “Iron” are conducted using D111-type apparatus, and those with series of run number “M” are using D-DIA.

^aTemperature was dropped to ~ 400 K instantaneously and recovered to 723 K within a few seconds.

2.3. Stress and Strain Measurements

During the deformation experiments, synchrotron radiation was employed to observe in situ changes in the sample's strain and stress through a combination of imaging and diffraction data collections. To achieve this, the incident X-rays were first monochromatized to around 60 keV using a Si (111) monochromator. A motorized stage with gadolinium aluminum gallium garnet (GAGG) or yttrium aluminum garnet (YAG) scintillators coupled to a CMOS or CCD camera was used to capture X-ray radiographic images, with exposure times ranging from 1 to 30 s. Sample strain was calculated by analyzing the absorption contrast between the sample and Al_2O_3 pistons (or the position of Au foil markers in some runs) in the X-ray radiographs (Figure 2a) using NIH Image-J software. The uniaxial strain was then determined using the formula $\epsilon = -\ln(l/l_0)$, where l and l_0 represent the sample length during and before deformation, respectively. An example of the strain changes during the Iron25 run is shown in Figure 2b. Furthermore, the strain rate ($\dot{\epsilon}$) during each experiment (and at each deformation step) was determined by fitting a linear equation to the series of strain–time data.

To calculate sample stress, two-dimensional angle-dispersive X-ray diffraction was used. The monochromatic X-rays were collimated using horizontal and vertical slits mounted on a motorized stage, with a size of $200 \times 200 \mu\text{m}$ or smaller depending on the sample shape and anvil gap width. Diffraction images were collected using a CMOS flat-panel detector (Dexela 2923, sensitive area of $291 \text{ mm} \times 230 \text{ mm}$, pixel size of 0.075 mm) or a CCD detector (MarCCD, sensitive area of 200 mm diameter circle, pixel size of 0.050 mm) at a distance of $541\text{--}641 \text{ mm}$ from the sample with an exposure time of 60–600 s. To calibrate incident X-ray energy and sample-detector geometry, a CeO_2 standard was placed at the sample position prior to high-pressure runs. Examples of the two-dimensional X-ray diffraction images in the experiments using D111-type and D-DIA apparatuses are shown in Figures 3a and 3b, respectively.

Four distinct diffraction peaks of hcp-Fe ($10\bar{1}0$, 0002, $10\bar{1}0$, and $10\bar{1}2$) were used to analyze stress and pressure. Each diffraction image was subdivided into 36 azimuthal sectors with equal azimuth angles η of 10° , and integrated separately using a software IPAnalyzer (Seto et al., 2010). Position of the sample diffraction peaks in each azimuthal bin were determined by fitting a symmetric pseudo-Voigt function to each integrated one-dimensional diffraction pattern using PDIndexer (Seto et al., 2010). This allows determination of the d spacings from sample diffraction peaks as a function of diffraction azimuth. Stress in the uniaxial deformation experiments was subsequently determined by fitting the following equation (e.g., Nye, 1985; Singh, 1993; Singh et al., 1998; Uchida et al., 1996);

$$d_{hkl}(\psi) = d_{hkl}^0 \left\{ 1 + (1 - 3 \cos^2 \psi) \frac{\sigma}{6(G_{hkl})} \right\} \quad (1)$$

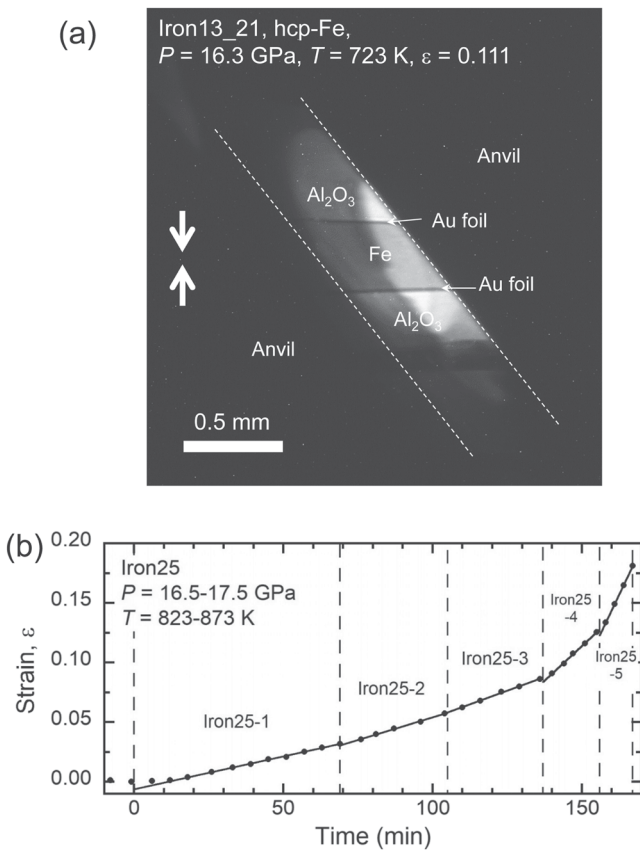


Figure 2. (a) X-ray radiograph at $P = 16.3 \text{ GPa}$ and $T = 723 \text{ K}$ with $\epsilon = 0.111$ during deformation in run Iron13 with D111-type apparatus. Sample and Al_2O_3 pistons were visible through diagonal anvil gap (dashed lines indicate anvil surface). We determined sample strain from distance of Au foil strain markers, which we placed at the top and bottom ends of sample. (b) Plot of strain versus time for run Iron25. Run Iron25 included five tests at three different temperatures of 823 (step 1), 848 (step 2), and 873 (steps 3–5) K at nearly constant pressure ($P = 16.5\text{--}17.5 \text{ GPa}$). In steps 3–5, strain rate was changed stepwise.

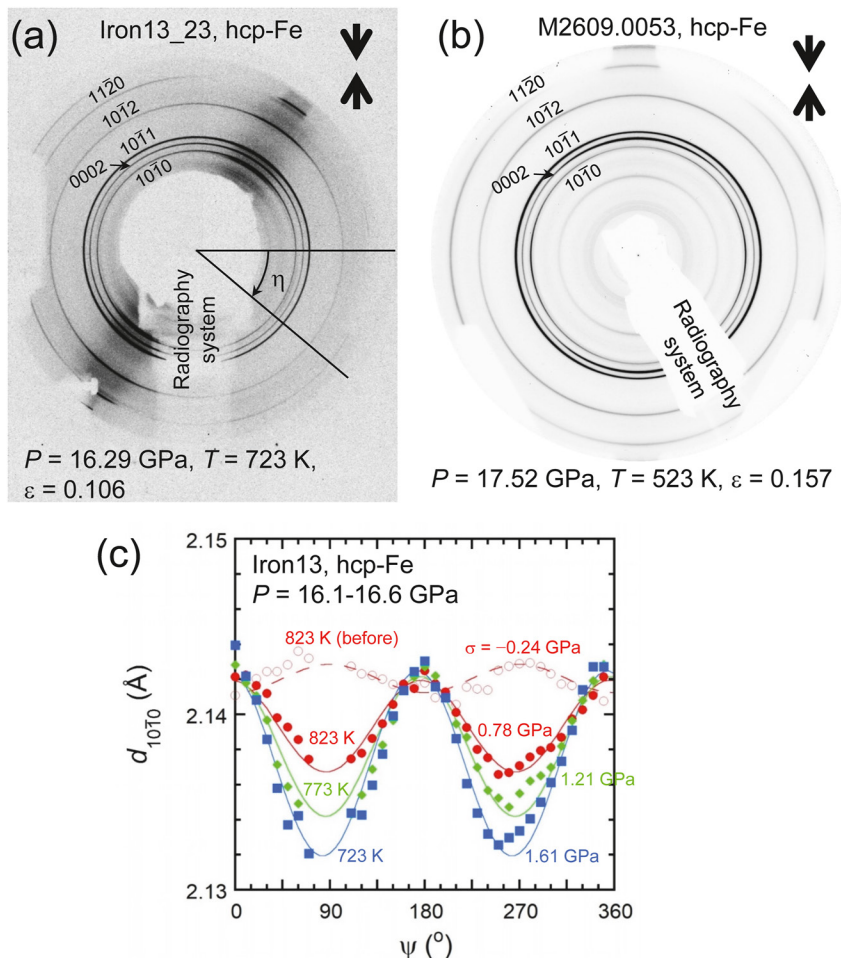


Figure 3. Two-dimensional X-ray diffraction images of hcp-Fe (a) at $P = 16.29$ GPa and $T = 723$ K with $\varepsilon = 0.106$ during deformation in run Iron13 using D111-type apparatus and (b) at $P = 17.52$ GPa and $T = 523$ K with $\varepsilon = 0.157$ during deformation in run M2609 using D-DIA apparatus. Compression direction is vertical. In (a), Diffraction Debye rings were more intense at angles corresponding to anvil gap (from top right to bottom left). In (b), the 0002 diffraction is more intense at top and bottom whereas the 1010 diffraction is at right and left which suggests basal plane normal is preferentially oriented to compression axis. (c) Variation in d spacing of hcp-Fe $10\bar{1}0$ for run Iron13 at $P = 16.1-16.6$ GPa. Open red circles, before deformation at $T = 823$ K; solid red circles, green diamonds, and blue squares, during deformation at 823, 773, and 723 K, respectively.

where ψ is the angle between the direction normal to the diffracting plane and the maximum principal stress direction, $d_{hkl}(\psi)$ is the observed d spacing as a function of the ψ angle, d_{hkl}^0 is the d spacing corresponding to the hydrostatic pressure; σ is the uniaxial stress calculated for a given diffraction peak with the Miller index hkl , and $\langle G_{hkl} \rangle$ is the effective shear modulus for a given hkl at the corresponding $P-T$ condition. The relationship between the angles η and ψ is expressed by $\cos \psi = \cos \theta \cos(\eta - \eta_{\max})$ where θ is the diffraction angle, and η_{\max} is the η angle at which $d_{hkl}(\psi)$ is the minimum (corresponding to the maximum principal stress direction) (see Merkel et al., 2002). Figure 3c shows examples of $d_{hkl}(\psi)-\psi$ data and the fits of Equation 1. The $\langle G_{hkl} \rangle$ term was calculated from the elastic constants (C_{ij}) of hcp-Fe at corresponding $P-T$ conditions using equations described by Singh et al. (1998). We assume a uniform stress condition in the calculation of $\langle G_{hkl} \rangle$ ($\alpha = 1$ in Equation 4 of Singh et al., 1998) and calculated the C_{ij} terms at high- P and high- T conditions based on Sha and Cohen (2010a, 2010b). The pressure was calculated by using the unit cell volume of iron, which was obtained from the d_{hkl}^0 values, extracted from the fitted azimuthal patterns (Equation 1), and the thermal equation of state of hcp-Fe as reported in Uchida et al. (2001) and Sakamaki et al. (2009).

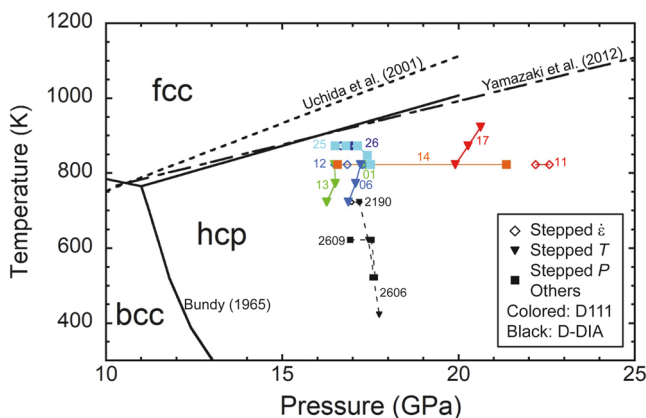


Figure 4. P - T conditions of deformation experiments. Open diamonds, inverse triangles, and squares, conditions of stepped strain rate, stepped temperature, and stepped pressure tests, respectively. Colored and black symbols, experiments using D111-type and D-DIA apparatus, respectively. Attached numbers denote run numbers. Thick black lines denote phase boundaries in Fe (Bundy, 1965; Uchida et al., 2001; Yamazaki et al., 2012).

axis. Similar observation was reported by Nishihara et al. (2018). Development of texture suggests dislocation glide played important role in these experiments. In the experiments using D111-type apparatus, observation of texture developed throughout deformation is more challenging. This is because of the larger anvils required in D111 experiments, the intensity difference between X-ray only transiting the anvil gap and those passing through cBN or sintered diamond anvils is far larger, which obscures intensity variations originating from sample texture.

3.3. Mechanical Results

Figure 5 shows the variations in stress and pressure during selected deformation experiments. The pressure was approximately constant in all deformation steps. Steady state was generally achieved after deformation with a strain (ϵ) of 0.02 in each step. In the steady-state deformation, applied stress and microstructure are regarded to be dynamically balanced with combination of concurrent processes such as dislocation glide, dynamic recrystallization and recovery maintaining equilibrium. The steady-state stress value in each run increased with increasing strain rate and pressure and decreasing temperature. The stress values calculated from four diffraction peaks differed, especially at higher-stress conditions, where the stress value by $10\bar{1}0$ was always the highest and that by $10\bar{1}2$ was generally the lowest among the four peaks. This tendency is consistent with that reported in previous studies (Merkel et al., 2012; Nishihara et al., 2018; Nishiyama et al., 2007). The difference of stress values between diffraction peaks primarily corresponds to difference in magnitude of the lattice distortion, and is also partly influenced by difference in $\langle G_{hkl} \rangle$ value (elastic anisotropy). This is due to the heterogeneous stress-strain distribution in the polycrystalline specimen caused by plastic anisotropy (orientation dependence of viscosity) (e.g., Castelnau et al., 2008). In M2190-2, during deformation at 723 K, the temperature instantaneously dropped ~ 400 K for a few seconds and then recovered to 723 K, possibly due to deformation or buckling of the graphite heater. We used the data obtained in M2190-2 for the following analysis because no remarkable change occurred in the strain or stress behavior before and after the drop and recovery in temperature. For Iron17-1, we performed deformation at 923 K, the highest temperature achieved in this study, but at these conditions the steady state stress was observed to be below the detection limits.

Figure 6a shows a log-log plot of the strain rate versus stress in the stepped strain rate tests (note that the error bars in Figures 6a, 6b, and 7a–7d represent the range of stresses determined by four diffraction peaks, not stress uncertainties). In these tests, we determined steady-state stress at different strain rates under a constant temperature and nearly constant pressure. Differential sample stress is observed to be temperature dependent; stress was ~ 2 GPa at 523 K and decreased with increasing temperature to 0.3–0.5 GPa at 873 K. The data from each run mostly showed power-law behavior (i.e., $\dot{\epsilon} \propto \sigma^n$). The slope of varying stress exponent (n) is indicated in the lower right of Figure 6a. Stress exponents of ~ 3 –5 were observed at temperatures higher than ~ 800 K and, whereas n

3. Results

3.1. Experimental Conditions

Table 1 summarizes the conditions and results of the deformation experiments. Figure 4 compares the P - T conditions of the deformation experiments with the stability field of hcp-Fe. We primarily conducted the deformation experiments in the high-temperature region of the stability field of hcp-Fe in the studied pressure range. The obtained data mostly fell within at $P \sim 17$ GPa with a few points at higher pressures up to 23 GPa. The bcc-Fe starting material was partially or completely transformed to hcp-Fe after compression at 300 K in all experiments, except for run M2609. The sample completely transformed, within the detection limits of the diffraction images, into an hcp structure during annealing at >723 K in all runs.

3.2. Texture Development

Development of texture was observed in the D-DIA experiments. Figure 3b shows two-dimensional X-ray diffraction image taken at the final stage of deformation in M2609. The Debye ring of 0002 diffraction is more intense at top and bottom whereas that of $10\bar{1}0$ diffraction is at right and left suggesting basal plane normal is preferentially oriented subparallel to the compression

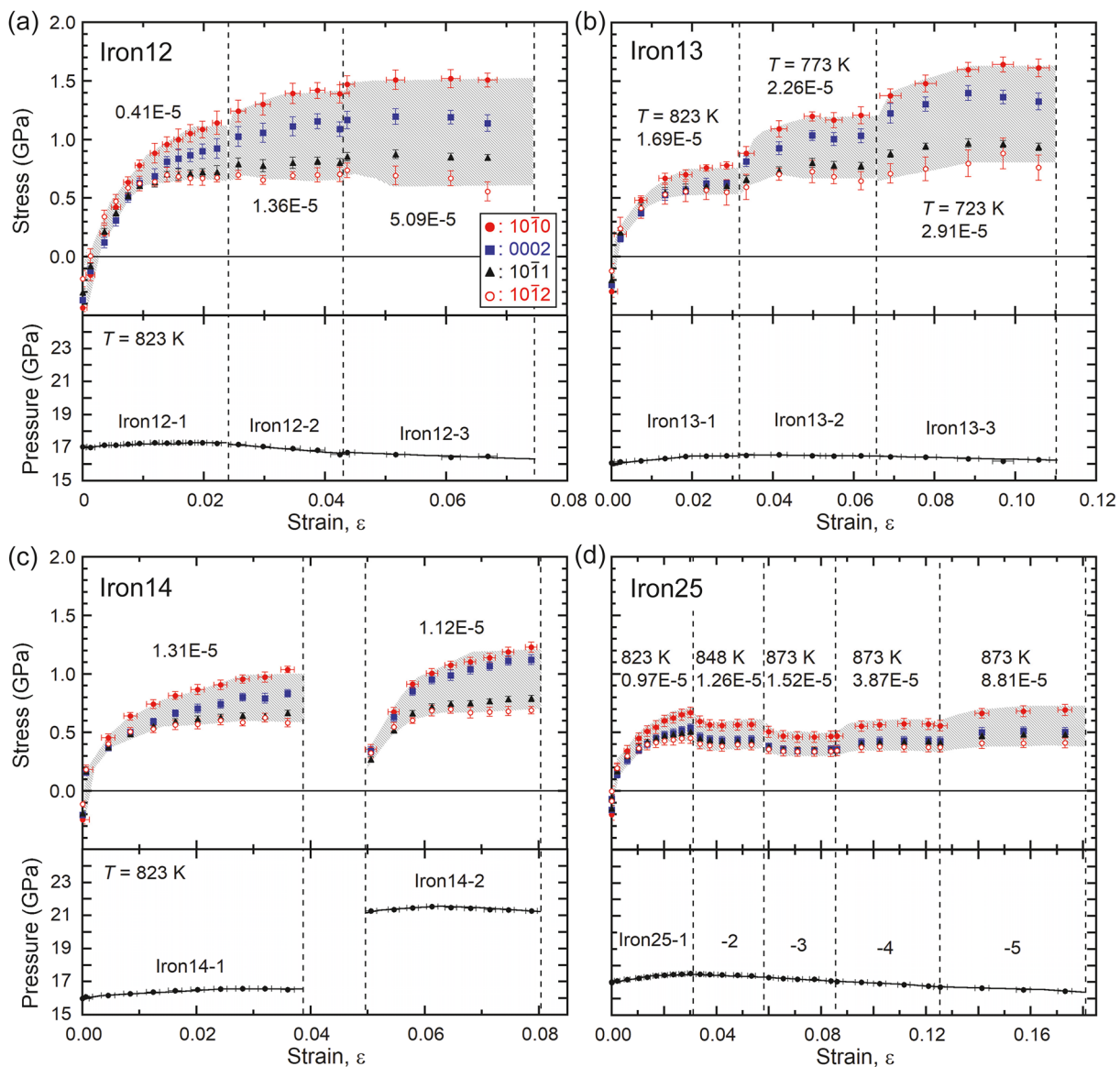


Figure 5. Plots of stress and pressure versus strain from deformation experiments (a) Iron12 (stepped strain rate test), (b) Iron13 (stepped temperature test), (c) Iron14 (stepped pressure test), and (d) Iron25 (stepped temperature and strain rate test). Each experiment included two or more deformation steps under different conditions. Error bars for stress values represent errors in the fitting of Equation 1. Attached numbers for each deformation step are strain rate in s^{-1} .

appears to be >5 at lower temperatures. The stress values previously reported by Nishiyama et al. (2007) at lower temperatures (400 and 600 K) and $P = 15.9\text{--}17.5 \text{ GPa}$ are consistent with our data at similar temperatures and strain rate (crosses in Figure 6a). The stress exponent obtained at 600 K by Nishiyama et al. (2007) ($n \sim 6$) was lower than that obtained in this study ($n > 10$). This could have been related to the extremely strong preferred orientation in Nishiyama et al.'s (2007) experiments where bcc-Fe rod was employed as a starting material.

Figure 6b shows the Arrhenius plot of stress versus reciprocal temperature for the stepped temperature tests. Each of these tests was conducted at nearly constant strain rate and pressure. The slope of this plot is proportional to H^*/n , where H^* is the activation enthalpy. Above $\sim 800 \text{ K}$, the H^*/n value was $\sim 60 \text{ kJ/mol}$, judging from the steep slope in the plot. At lower temperatures, the H^*/n value drastically decreased with decreasing temperature. The changes in temperature dependence and n value (Figure 6a) consistently suggested a transition in the deformation mechanism at $\sim 800 \text{ K}$.

Figure 6c is a semilog plot of stress versus pressure for the stepped pressure test (Iron14) at a constant temperature of 823 K and nearly constant strain rate of $1.1\text{--}1.3 \times 10^{-5} \text{ s}^{-1}$. The steady-state stress values at $P = 21.4 \text{ GPa}$

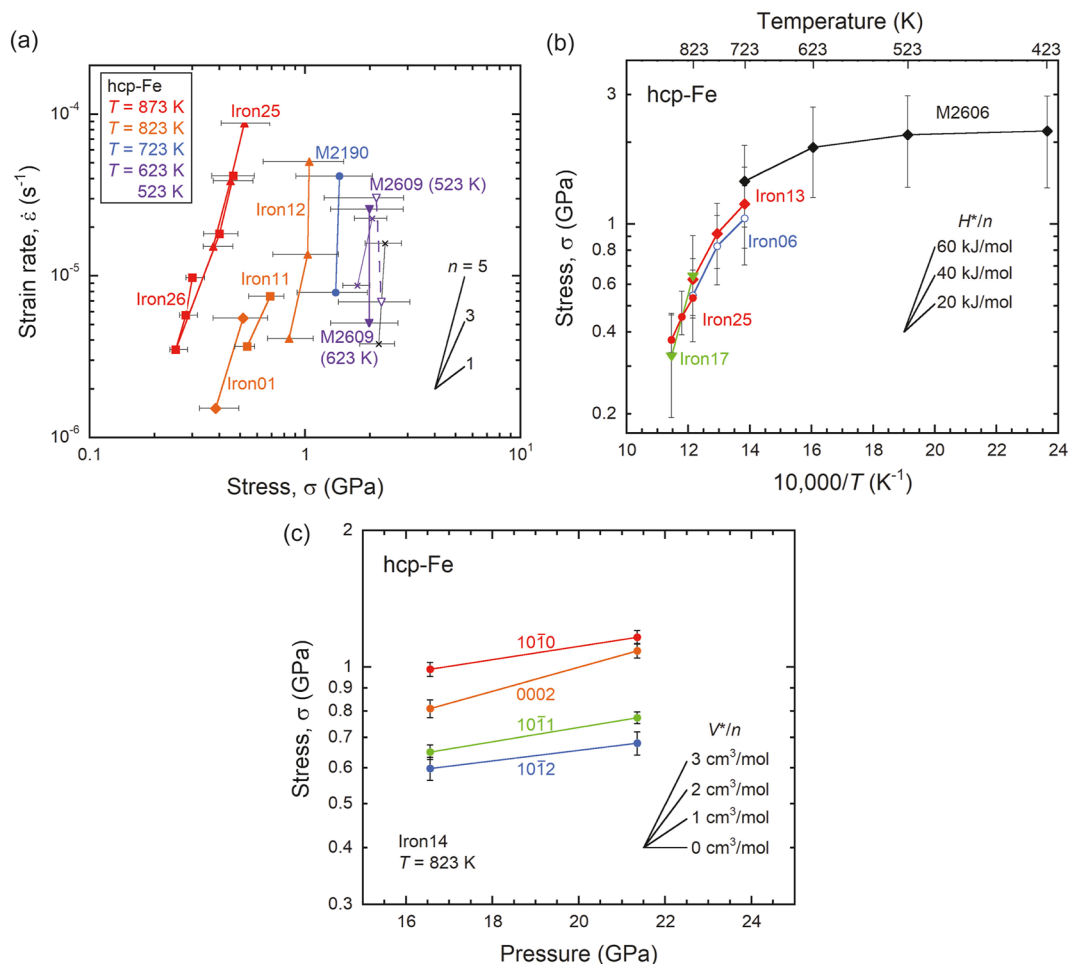


Figure 6. Plots of mechanical results. (a) Log-log plot of strain rate versus stress for stepped strain rate tests. (b) Semilog plot of stress versus reciprocal temperature for stepped temperature tests. (c) Semilog plot of stress versus pressure for stepped pressure test. Symbols and error bars represent averages and ranges, respectively, of steady-state stress determined from four diffraction peaks (10̄10, 0002, 10̄11, and 10̄12) except for those in (c). Purple and black crosses in (a) are data at 600 and 400 K, respectively, at 15.9–17.5 GPa reported by Nishiyama et al. (2007) for which stress values are the average of those of 10̄10 and 10̄11.

were slightly higher than those at $P = 16.6$ GPa. Although the pressure dependence of the stress slightly differed depending on the diffraction peaks, the slopes indicated in this plot are generally gentle suggesting that the V^*/n value was substantially lower than $1 \text{ cm}^3/\text{mol}$ (V^* is the activation volume).

The mechanical data for each run were not fully consistent owing to the run-to-run variability. The most notable example is shown in Figure 6a: the stress values of runs Iron01 and Iron12 differed by a factor of ~ 2 at a strain rate of $\sim 4 \times 10^{-6} \text{ s}^{-1}$, although we conducted both these runs at the same temperature (823 K) and pressure (16.4–17.4 GPa). One possible reason for this run-to-run variability is the run-to-run difference in the position of the thermocouple junction. Even though the design of the cell assembly (Figure 1) was practically identical throughout this study, a small change in the position of the thermocouple junction could have occurred. This could have led to a systematic difference in the temperature from run to run. Another explanation for the run-to-run variability is the run-to-run difference in hydrogen content (e.g., Hayashi et al., 1998). Although we conducted the experiments under nominally anhydrous conditions, a small amount of water may have adsorbed to the pressure medium from the moisture in the air and hydrogen may have been incorporated in sample. Because rheology can be highly sensitive to differences in the chemical and physical environments, run-to-run variability is unavoidable. However, the data derived in a single run would be consistent because the chemical and physical environments remain essentially unchanged in a single run. Therefore, run-to-run variability must be corrected to accurately determine flow law parameters and deformation mechanisms.

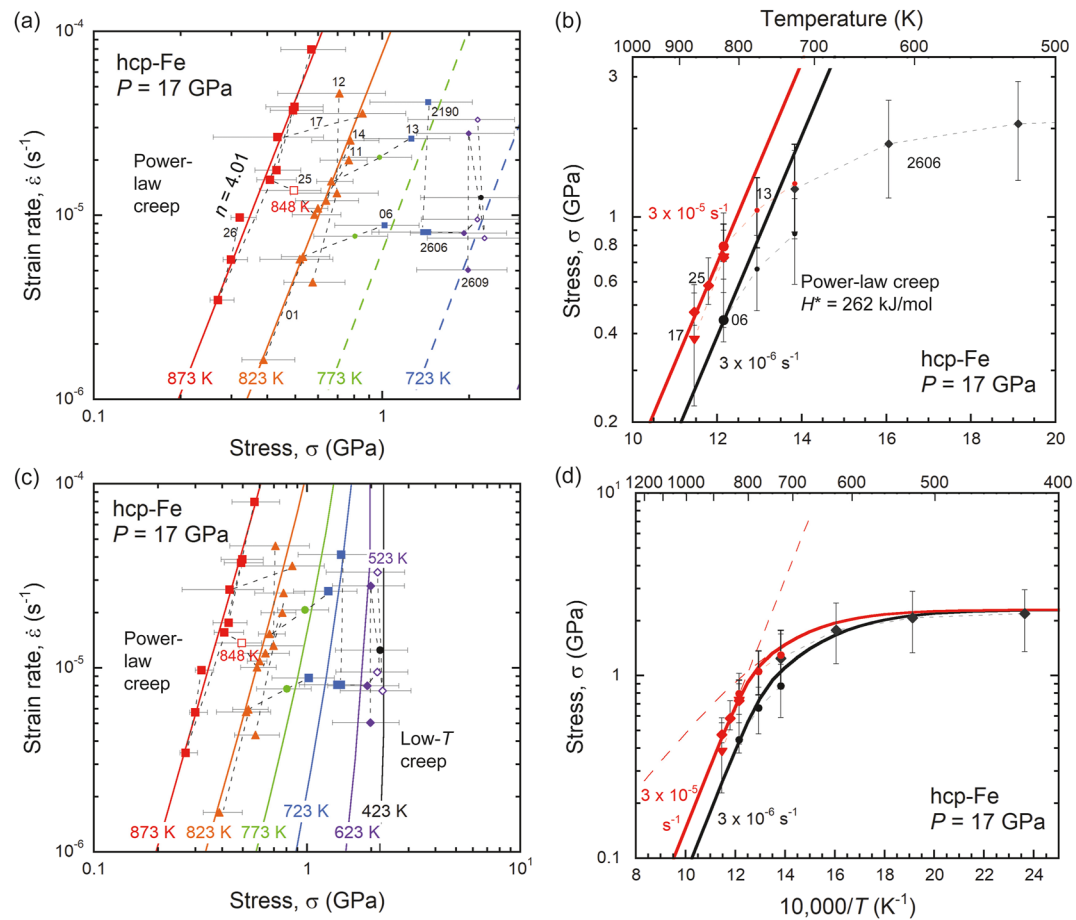


Figure 7. Results of (a, b) fit of flow-law equation for power-law creep (Equation 3) to data at $T = 823\text{--}873$ K; (c, d) a simultaneous fit of flow-law equations for power-law creep and low- T creep (Equation 4) to all data. All data were after stress correction for run-to-run variability, and were normalized to $P = 17$ GPa using parameters determined by fit of flow-law equations. Fit of flow-law equations is expressed by thick lines. Data of individual runs are connected by thin black dashed lines. (a, c) Log-log plots of strain rate versus stress including all data as symbols. Symbol and color indicate temperature. (b, d) Semi-log plots of stress versus reciprocal temperature including only data in stepped temperature tests as symbols for clarity. Experimental data were normalized to $\dot{\epsilon} = 3 \times 10^{-6}$ (black) or 3×10^{-5} (red) s^{-1} . Attached small black numbers in (a, b) denote run numbers.

4. Discussion

4.1. Interpretation of Rheological Behavior

As described above, the mechanical data of hcp-Fe suggests the occurrence of differing mechanisms at temperatures above and below ~ 800 K (Figures 6a and 6b). Based on this observation, we analyzed the mechanical data at >800 K and <800 K separately.

At >800 K, the observed stress exponent was $n \sim 3\text{--}5$ (Figure 6a), which is in the range of common values for the power-law dislocation creep of metals (e.g., Mukherjee, 2002). The constitutive equation for power-law dislocation creep is:

$$\dot{\epsilon} = A_{PL} \sigma^{n_{PL}} \exp\left(-\frac{E_{PL}^* + PV_{PL}^*}{RT}\right) \quad (2)$$

where $\dot{\epsilon}$ is the strain rate, A is the pre-exponential constant, σ is the deviatoric stress, E^* is the activation energy, V^* is the activation volume, and R is the gas constant. The subscript PL represents parameters for power-law dislocation creep. For successful data analysis via Equation 2, the observed run-to-run variability needed to be corrected. This was achieved using a similar approach to that used by Keefner et al. (2011), developed to

Table 2
Flow Law Parameters

Parameters	Power-law creep (PL)	Low-T creep (LT)
$\log_{10} A$	($s^{-1} \text{ GPa}^{-n}$)	12.50 ± 1.6
n		4.0 ± 0.3
E^*	(kJ/mol)	240 ± 20
V^*	(cm^3/mol)	1.4 ± 0.2
σ_p	(GPa)	-
p		2.3
q		-
		1
		0.1

^aParameters for boundary diffusion coefficient after Brown and Ashby (1980).

Parameters for power-law and low-T creeps are for Equations 2 and 4, respectively. See text for details.

analyze deformation experiments on olivine aggregates in a dislocation creep regime at $P = 300$ MPa. In this study the authors precisely determined the flow-law parameters using a global fit of the constitutive equation to derived mechanical data with a correction for run-to-run variability by multiplying the pre-exponential constant, A , by parameter, α , where α differs between runs. We adopted similar correction approach in this study, but instead of correcting pre-exponential factor, A , we applied a run-to-run correction on the observed stress, σ_{obs} . The correction parameter, β , was used such that the corrected stress (σ_{cor}) is determined as $\sigma_{\text{cor}} = \beta \times \sigma_{\text{obs}}$. Therefore, Equation 2 becomes:

$$\dot{\epsilon} = A_{\text{PL}}(\beta \sigma_{\text{obs}})^{n_{\text{PL}}} \exp\left(-\frac{E_{\text{PL}}^* + PV_{\text{PL}}^*}{RT}\right). \quad (3)$$

where β differs for each run, but is close to one when the run-to-run variability is small. The correction was applied to stress rather than pre-exponential constant in this study because, in the case of $n > 1$, as in this study, the required correction magnitude becomes smaller when a correction is applied to stress.

Equation 3 was fitted to the data at high temperatures (>800 K) whereby the values of β for all runs were simultaneously adjusted to minimize $\sum_i (\log \beta_i)^2$ (β_i is β for a run i) providing the best fitting β values close to one. Fitting results are shown in Figures 7a and 7b. The derived flow-law parameters and β values are presented in Table 2 and Table S1 in Supporting Information S1, respectively. The stress correction parameter β ranged between 0.678 and 1.332. These corrections are equivalent to temperature deviations of +39 to -27 K (at 873 K and 17 GPa) assuming that the entirety of the run-to-run variability is attributable to the temperature errors. The determined flow-law parameters are $n = 4.0 \pm 0.3$, $E^* = 240 \pm 20$ kJ/mol, and $V^* = 1.4 \pm 0.2$ cm^3/mol . Activation enthalpy, H^* ($= E^* + PV^*$), at $P = 17$ GPa was calculated to be 260 ± 20 kJ/mol. These values suggest that the dominant deformation mechanism of hcp-Fe at >800 K is dislocation creep, the rate-limiting process of which is dislocation climb (Weertman creep). The stress exponent ($n = 4.0$) falls within the range of typical Weertman creep values of hcp metals, $3.0 \leq n \leq 5.5$ (Mukherjee, 2002).

In Weertman creep, the activation enthalpy, and hence the activation energy and volume, are comparable to that of lattice diffusion (e.g., Frost & Ashby, 1982). Although no experimental study has been published on the diffusion coefficient for the lattice diffusion of hcp-Fe, Ritterbex and Tsuchiya (2020) calculated the self-diffusion coefficient of hcp-Fe based on density functional theory. Their results included an H^* at $P = 17$ GPa and V^* of 500 kJ/mol and 3.0 cm^3/mol , respectively, for hcp-Fe. These values are considerably higher than those obtained for power-law creep at >800 K in this study. On the other hand, the H^* of hcp-Fe at 17 GPa was estimated to be 290 kJ/mol based on a universal relationship between the melting temperature and diffusion coefficient for hcp metals (Brown & Ashby, 1980) using the fictive melting temperature of hcp-Fe at 17 GPa as 1990 K (Anderson & Isaak, 2000), which is fairly consistent with the results of this study.

The diffusion coefficient for the lattice diffusion of hcp-Fe is generally assumed to be close to that of fcc-Fe because both hcp and fcc are close-packed structures. E^* for self-diffusion in fcc-Fe is approximately 270 kJ/mol (Frost & Ashby, 1982). Based on high-pressure experiments by Yunker and Van Orman (2007), H^* and V^* at $P = 17$ GPa for Fe-Ni inter-diffusion in a fcc-structured Fe-Ni alloy were determined to be 365 kJ/mol and 3.1 cm^3/mol , respectively. Compared with the activation parameters of diffusion for fcc-Fe, the E^* , H^* , and V^* values of the power-law dislocation creep of hcp-Fe in this study are consistent (E^*) or somewhat lower. Therefore, although we are not fully certain that the power-law creep at >800 K in this study was rate-limited by dislocation climb and hence lattice diffusion, it is our preferred interpretation that the observed deformation mechanism was Weertman creep, which may be dominant at higher temperatures near the melting temperature.

At temperatures lower than 800 K, the stress exponents were larger (Figure 6a), and the temperature dependence of the deviatoric stress was smaller (Figure 6b). The most common low-temperature deformation mechanism in metals is a type of power-law creep (e.g., Frost & Ashby, 1982) whereby diffusion along the dislocation line (pipe diffusion) is the rate-limiting process. At low temperatures, a power-law breakdown is commonly observed,

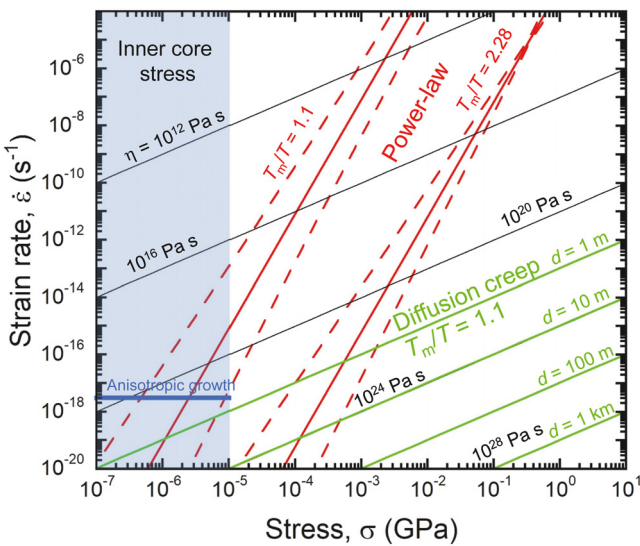


Figure 8. Extrapolation of flow-law of hcp-Fe for power-law creep to inner core conditions. Red lines are calculated stress–strain rate relationship for power-law creep at $T_m/T = 2.28$ and 1.1 based on our study ($T_m/T = 2.28$ corresponds to $T = 873$ K at 17 GPa). Dashed lines indicate range of 95% confidence level of extrapolation. Green lines are diffusion creep at $T_m/T = 1.1$ with grain size of $d = 1, 10, 100$, and 1 km calculated using Equation 6 and diffusion coefficient by Yunker and Van Orman (2007). Thin black lines are isopleths for viscosity (η) of $10^{12}, 10^{16}, 10^{20}, 10^{24}$, and 10^{28} Pa s . Light blue area indicates range of stress in inner core, $<10^4\text{ Pa}$ (Buffett, 1997; Karato, 1999; Yoshida et al., 1996). Thick blue line represents strain rate in inner core produced by equatorial inner core growth (Yoshida et al., 1996).

normalized pressure of 17 GPa. Assuming that the mechanisms at high and low temperatures were independent, the total strain rate could be expressed as the sum of the strain rates of the two mechanisms (Equations 3 and 4). As shown in these figures, the flow-law equations provide good fits to the experimental observations from this study, suggesting the above analysis was appropriate.

4.2. Implications for Inner Core Viscosity

Based on the above findings, the high-temperature deformation mechanism (power-law dislocation creep), assuming there are no pressure-induced changes in deformation mechanism, may be the dominant mechanism in the Earth's inner core. Making this assumption the above determined flow law was extrapolated to conditions of the inner core based on homologous temperature scaling (Figure 8). In the homologous temperature scaling, the activation enthalpy is expressed through melting temperature (T_m) as $H^* = gRT_m$, where g is semi-empirical constant (e.g., Brown & Ashby, 1980). By substituting gRT_m for $E^* + PV^*$ ($= H^*$) in Equation 2, the following equation can be used in the extrapolation:

$$\dot{\epsilon} = A_{PL}\sigma^{n_{PL}} \exp\left(-g\frac{T_m}{T}\right). \quad (5)$$

The g value for hcp-Fe was determined to be 15.8 using values of H^* and T_m at $P = 17\text{ GPa}$ (260 kJ/mol and 1990 K (Anderson & Isaak, 2000), respectively). Extrapolation of this relationship was undertaken to a commonly accepted inner core temperature of $T_m/T = 1.1$ and a stress of 10^2 Pa ($= 10^{-7}\text{ GPa}$) because the inner core stress has generally been regarded as $\leq 10^4\text{ Pa}$ (e.g., Buffett, 1997; Karato, 1999; Yoshida et al., 1996).

To evaluate the possible contribution of diffusion creep (Nabarro–Herring creep), we calculated the stress–strain rate relationship at $T_m/T = 1.1$ using a rate equation (e.g., Karato, 2008) with the reported diffusion coefficient of fcc-Fe (Yunker & Van Orman, 2007). As shown in Figure 8, the strain rate of diffusion creep for grain size (d)

where the stress exponent is no longer constant (e.g., Frost & Ashby, 1982). The power-law breakdown is commonly recognized as transition of mechanism from dislocation climb-controlled flow to dislocation glide-controlled flow. The constitutive equation for low-temperature power-law creep with a power-law breakdown is:

$$\dot{\epsilon} = A_{LT}\sigma_{cor}^{n_{LT}} \exp\left(-\frac{E_{LT}^* + PV_{LT}^*}{RT} \left\{ 1 - \left(\frac{\sigma_{cor}}{\sigma_p}\right)^p \right\}^q\right), \quad (4)$$

where σ_p is the Peierls stress; p and q are constants that are generally bounded as $0 \leq p \leq 1$ and $1 \leq q \leq 2$, respectively. The subscript LT represents parameters for the low- T mechanism. Equation 4 was fitted to the experimental data from this study at conditions of $<800\text{ K}$. Again the observed run-to-run variability was corrected using the stress correction parameter, β , as described above. β was fixed = 1 for runs M2606, 2609, and 2190, in which the temperature was $<800\text{ K}$ throughout the experiments. We assumed $n = 5$, which is a common value for the low-temperature power-law creep of metals. The E^* and V^* for the low-temperature mechanism, and hence pipe diffusion, were assumed to be close to those for grain-boundary diffusion (Frost & Ashby, 1982). We estimated the E^* and V^* for the low-temperature mechanism of hcp-Fe by multiplying the E^* and V^* for the high-temperature mechanism by 10.8/17.3 following the empirical relationship between Arrhenius parameters for grain-boundary diffusion and lattice diffusion presented by Brown and Ashby (1980) (Table 2). Values of A , σ_p , p , and q were manually adjusted to best fit the data, as automatic fitting algorithms were found to be unstable (Table 2). Although q is generally within the range of $1 \leq q \leq 2$, a small value ($q = 0.1$) was required to fit our experimental data. This drastically changes the temperature dependence of stress (Figure 6b).

Figures 7c and 7d show the fits of the flow-law equations of the high- and low-temperature mechanisms (power-law and low- T creeps, respectively) at a

of >1 m (e.g., Bergman, 1998; Yamazaki et al., 2017) is lower than that of power-law dislocation creep under the most probable stress range in the inner core, 10^3 – 10^4 Pa ($=10^{-6}$ – 10^{-5} GPa). Therefore, diffusion creep does not appear to be a dominant deformation mechanism in the Earth's inner core. This conclusion is reasonable because diffusion creep hardly yields crystallographic preferred orientation, and hence, it should not be able to explain the observed seismic anisotropy.

At the stress condition of $\leq 10^4$ Pa (Buffett, 1997; Karato, 1999; Van Orman, 2004; Yoshida et al., 1996), the viscosity and strain rate for power-law dislocation creep were calculated to be $\geq 10^{19.1 \pm 2.2}$ Pa s and $\leq 10^{-15.1 \pm 2.2}$ s $^{-1}$, respectively. According to Lasbleis and Deguen (2015), plume convection and tangential Lorentz force mechanisms do not appear when the inner core viscosity is $>10^{18}$ Pa s. Thus, if the power-law creep (following the flow law determined in this study) is dominant in the inner core, equatorial growth and translation mode are the viable candidates as the dominant geodynamic mechanisms. The equatorial growth mechanism has been regarded as one of the most probable candidates for the dominant inner core dynamics, by which formation of seismic anisotropy with several percent level can be reasonably explained under some conditions with compositional stratification, pretexture, or inner core translation (e.g., Frost et al., 2021; Lincot et al., 2016). Our conclusion supports this model.

Although we have assumed power-law creep, as inferred from experiments in this study, as a dominant deformation mechanism in the above discussion, other deformation mechanisms are also possibly dominant in the Earth's inner core. Harper–Dorn creep is often regarded as the dominant deformation mechanism in the inner core (e.g., Tsujino et al., 2020; Van Orman, 2004), which appears under low stress and large-grain conditions, but its mechanism is not fully understood, and its existence has been the subject of debate (e.g., Kassner et al., 2007). If Harper-Dorn creep is the dominant deformation mechanism, the inner core viscosity may be lower than the above estimate, and thus the discussion on the Earth's inner core dynamics could be revised.

We also note that throughout the above discussion a rheology relevant for pure Fe, neglecting the effect of compositional variation, has been assumed representative of the inner core. However, incorporation of light element(s) (e.g., H, Si, S) can have potentially significant influence on the rheology of hcp-Fe. Further studies investigating this issue are desirable for accurate understanding of the inner core dynamics.

5. Conclusion

Rheology of hcp-Fe was determined via uniaxial deformation experiments performed using D111-type and D-DIA apparatuses at $P = 16.3$ – 22.6 GPa, $T = 423$ – 923 K. The results showed that the dominant deformation mechanism in hcp-Fe changes depending on the temperature, with power-law dislocation creep and low-temperature creep dominate above and below ~ 800 K, respectively. An extrapolation of the derived flow law for power-law dislocation creep based on homologous temperature scaling suggested that the viscosity of hcp-Fe under inner core conditions is $\geq \sim 10^{19}$ Pa s. If the power-law dislocation creep is assumed to be the dominant mechanism in the Earth's inner core, the equatorial growth or translation mode mechanism may be the dominant geodynamical mechanism.

Data Availability Statements

The data sets for this study are available at <https://doi.org/10.5281/zenodo.7273263>.

References

- Alfè, D., Gillan, M. J., & Price, G. D. (2002). Composition and temperature of the Earth's core constrained by combining ab initio calculations and seismic data. *Earth and Planetary Science Letters*, 195(1–2), 91–98. [https://doi.org/10.1016/S0012-821X\(01\)00568-4](https://doi.org/10.1016/S0012-821X(01)00568-4)
- Anderson, O. L., & Isaak, D. G. (2000). Calculated melting curves for phases of iron. *American Mineralogist*, 85(2), 376–385. <https://doi.org/10.2138/am-2000-2-317>
- Birds, J., Côté, A. S., & Brodholt, J. P. (2014). A seismologically consistent compositional model of Earth's core. *Proceedings of the National Academy of Sciences*, 111(21), 7542–7545. <https://doi.org/10.1073/pnas.1316708111>
- Bergman, M. I. (1998). Estimates of the Earth's inner core grain size. *Geophysical Research Letters*, 25(10), 1593–1596. <https://doi.org/10.1029/98GL01239>
- Birch, F. (1952). Elasticity and constitution of the Earth's interior. *Journal of Geophysical Research*, 57(2), 227–286. <https://doi.org/10.1029/JZ057002p00227>
- Brett, H., & Deuss, A. (2020). Inner core anisotropy measured using new ultra-polar PKIKP paths. *Geophysical Journal International*, 223(2), 1230–1246. <https://doi.org/10.1093/gji/ggaa348>

Acknowledgments

We thank A. Suzuki, T. Kubo, and N. Funamori for their helpful support with the in situ deformation experiments, and T. Ohuchi and S. Ritterbex for their constructive discussions. We also thank E. Takahashi for providing sintered diamond anvils, and K. Nishida, and R. Iizuka-Oku for developing the X-ray radiograph system at KEK. In situ deformation experiments were performed using a D111-type system at NE7A, PF-AR at KEK (proposal numbers 2016G016, 2017PF-02, 2017PF-07, and 2018G059) and the SPEED-MkII-D system at BL04B1 in SPring-8 (proposal numbers 2017A0075 and 2018B0075). This study was supported by the Japan Society for the Promotion of Science (JSPS) under Grant-in-Aid for Scientific Research (A) (19H00723) and (B) (15H03749), and Grant-in-Aid for Innovative Areas (15H05827). Constructive comments by J. Van Orman and an anonymous reviewer are appreciated.

- Brown, A. M., & Ashby, M. F. (1980). Correlations for diffusion constants. *Acta Metallurgica*, 28(8), 1085–1101. [https://doi.org/10.1016/0001-6160\(80\)90092-9](https://doi.org/10.1016/0001-6160(80)90092-9)
- Buffett, B. A. (1997). Geodynamic estimates of the viscosity of the Earth's inner core. *Nature*, 388(6642), 571–573. <https://doi.org/10.1038/41534>
- Buffett, B. A., & Wenk, H.-R. (2001). Texturing of the Earth's inner core by Maxwell stresses. *Nature*, 413(6851), 60–63. <https://doi.org/10.1038/35092543>
- Bundy, F. P. (1965). Pressure-temperature phase diagram of iron to 200 kbar, 900°C. *Journal of Applied Physics*, 36(2), 616–620. <https://doi.org/10.1063/1.1714038>
- Castelnau, O., Blackman, D. K., Lebensohn, R. A., & Castaneda, P. P. (2008). Micromechanical modeling of the viscoplastic behavior of olivine. *Journal of Geophysical Research*, 113(B9), B09202. <https://doi.org/10.1029/2007JB005444>
- Creager, K. C. (1992). Anisotropy of the inner core from differential travel times of the phases PKP and PKIKP. *Nature*, 356(6367), 309–314. <https://doi.org/10.1038/356309a0>
- Frost, D. A., Lasbleis, M., Chandler, B., & Romanowicz, B. (2021). Dynamic history of the inner core constrained by seismic anisotropy. *Nature Geoscience*, 14(7), 531–535. <https://doi.org/10.1038/s41561-021-00761-w>
- Frost, H. J., & Ashby, M. F. (1982). *Deformation mechanism maps: The plasticity and creep of metals and ceramics*. Pergamon Press.
- Gleason, A. E., & Mao, W. L. (2013). Strength of iron at core pressures and evidence for a weak Earth's inner core. *Nature Geoscience*, 6(7), 571–574. <https://doi.org/10.1038/ngeo1808>
- Hayashi, E., Kurokawa, Y., & Fukai, Y. (1998). Hydrogen-induced enhancement of interdiffusion in Cu-Ni diffusion couples. *Physical Review Letters*, 80(25), 5588–5590. <https://doi.org/10.1103/PhysRevLett.80.5588>
- Hirose, K., Wood, B., & Vočadlo, L. (2021). Light elements in the Earth's core. *Nature Reviews Earth & Environment*, 2(9), 645–658. <https://doi.org/10.1038/s43017-021-00203-6>
- Hunt, S. A., Weidner, D. J., McCormack, R. J., Whitaker, M. L., Bailey, E., Li, L., et al. (2014). Deformation T-cup: A new multi-anvil apparatus for controlled deformation experiments at pressures above 18 GPa. *Review of Scientific Instruments*, 85(8), 085103. <https://doi.org/10.1063/1.4891338>
- Jeanloz, R., & Wenk, H. R. (1998). Convection and anisotropy of the inner core. *Geophysical Research Letters*, 15(1), 72–75. <https://doi.org/10.1029/97GL015001p00072>
- Karato, S. (1999). Seismic anisotropy of the Earth's inner core resulting from flow induced by Maxwell stresses. *Nature*, 402(6764), 871–873. <https://doi.org/10.1038/47235>
- Karato, S. (2008). *Deformation of Earth materials: An introduction to the rheology of solid Earth*. Cambridge Univ. Press. <https://doi.org/10.1017/CBO9780511804892>
- Kassner, M. E., Kumar, P., & Blum, W. (2007). Harper-Dorn creep. *International Journal of Plasticity*, 23(6), 980–1000. <https://doi.org/10.1016/j.ijplas.2006.10.006>
- Kawazoe, T., Nishihara, Y., Ohuchi, T., Nishiyama, N., Higo, Y., Funakoshi, K., & Irfune, T. (2011). In situ stress-strain measurements in a deformation-DIA apparatus at P-T conditions of the upper part of the mantle transition zone. *American Mineralogist*, 96(11–12), 1665–1672. <https://doi.org/10.2138/am.2011.3818>
- Keefner, J. W., Mackwell, S. J., Kohlstedt, D. L., & Heidelbach, F. (2011). Dependence of dislocation creep of dunite on oxygen fugacity: Implications for viscosity variations in Earth's mantle. *Journal of Geophysical Research*, 116(B5), B05201. <https://doi.org/10.1029/2010JB007748>
- Lasbleis, M., & Deguen, R. (2015). Building a regime diagram for the Earth's inner core. *Physics of the Earth and Planetary Interiors*, 247, 80–93. <https://doi.org/10.1016/j.pepi.2015.02.001>
- Lincot, A., Cardin, P., Deguen, R., & Merkel, S. (2016). Multiscale model of global inner-core anisotropy induced by hcp alloy plasticity. *Geophysical Research Letters*, 43(3), 1084–1091. <https://doi.org/10.1002/2015GL067019>
- Merkel, S., Gruson, M., Wang, Y., Nishiyama, N., & Tomé, C. (2012). Texture and elastic strains in hcp-iron plastically deformed up to 17.5 GPa and 600 K: Experiment and model. *Modelling and Simulation in Materials Science and Engineering*, 20(2), 024005. <https://doi.org/10.1088/0965-0393/20/2/024005>
- Merkel, S., Wenk, H.-R., Gillet, P., Mao, H.-k., & Hemley, R. J. (2004). Deformation of polycrystalline iron up to 30 GPa and 1000 K. *Physics of the Earth and Planetary Interiors*, 145(1–4), 239–251. <https://doi.org/10.1016/j.pepi.2004.04.001>
- Merkel, S., Wenk, H. R., Shu, J., Shen, G., Gillet, P., Mao, H.-k., & Hemley, R. J. (2002). Deformation of polycrystalline MgO at pressures of the lower mantle. *Journal of Geophysical Research*, 107(B11), ECV3-1–ECV3-17. <https://doi.org/10.1029/2001JB000920>
- Miyagi, L., Kunz, M., Knight, J., Nasiatka, J., Voltolini, M., & Wenk, H.-R. (2008). *In situ* phase transformation and deformation of iron at high pressure and temperature. *Journal of Applied Physics*, 104(10), 103510. <https://doi.org/10.1063/1.3008035>
- Monnereau, M., Valvet, M., Margarin, L., & Souriau, A. (2010). Lopsided growth of Earth's inner core. *Science*, 328(5981), 1014–1017. <https://doi.org/10.1126/science.1186212>
- Morelli, A., Dziewonski, A. M., & Woodhouse, J. H. (1986). Anisotropy of the inner core inferred from PKIKP travel times. *Geophysical Research Letters*, 13(13), 1545–1548. <https://doi.org/10.1029/GL013013p01545>
- Mukherjee, A. K. (2002). An examination of the constitutive equation for elevated temperature plasticity. *Materials Science and Engineering*, 322(1–2), 1–22. [https://doi.org/10.1016/S0921-5093\(01\)01115-7](https://doi.org/10.1016/S0921-5093(01)01115-7)
- Nishihara, Y., Doi, S., Kakizawa, S., Higo, Y., & Tange, Y. (2020). Effect of pressure on temperature measurements using WRe thermocouple and its geophysical impact. *Physics of the Earth and Planetary Interiors*, 298, 106348. <https://doi.org/10.1016/j.pepi.2019.106348>
- Nishihara, Y., Ohuchi, T., Kawazoe, T., Seto, Y., Maruyama, G., Higo, Y., et al. (2018). Deformation-induced crystallographic-preferred orientation of hcp-iron: An experimental study using a deformation-DIA apparatus. *Earth and Planetary Science Letters*, 490, 151–160. <https://doi.org/10.1016/j.epsl.2018.03.029>
- Nishihara, Y., Tsujino, N., Kubo, T., Yamazaki, D., Doi, S., Imamura, M., & Yoshino, T. (2020). Studies of deep Earth rheology based on high-pressure deformation experiments using D111-type apparatus. *The Review of High Pressure Science and Technology*, 30(2), 78–84. (in Japanese with English abstract). <https://doi.org/10.4131/jshpreview.30.78>
- Nishiyama, N., Wang, Y., Rivers, M. L., Sutton, S. R., & Cookson, D. (2007). Rheology of ε-iron up to 19 GPa and 600 K in the D-DIA. *Geophysical Research Letters*, 35(23), L23304. <https://doi.org/10.1029/2007GL031431>
- Nye, J. F. (1985). *Physical properties of crystals* (p. 322). Oxford Univ. Press.
- Raterron, P., Merkel, S., & Holyoke, C. W. (2013). Axial temperature gradient and stress measurements in the deformation-DIA cell using alumina pistons. *Review of Scientific Instruments*, 84(4), 043906. <https://doi.org/10.1063/1.4801956>
- Reaman, D. M., Colijin, H. O., Yang, F., Hauser, A. J., & Panero, W. R. (2012). Interdiffusion of Earth's core materials to 65 GPa and 2200 K. *Earth and Planetary Science Letters*, 349–350, 8–14. <https://doi.org/10.1016/j.epsl.2012.06.053>
- Ritterbex, S., & Tsuchiya, T. (2020). Viscosity of hcp iron at Earth's inner core conditions from density functional theory. *Scientific Reports*, 10(1), 6311. <https://doi.org/10.1038/s41598-020-63166-6>

- Romanowicz, B., Cao, A., Godwal, B., Wenk, R., Ventosa, S., & Jeanloz, R. (2016). Seismic anisotropy in the Earth's innermost inner core: Testing structural models against mineral physics predictions. *Geophysical Research Letters*, 43(1), 93–100. <https://doi.org/10.1002/2015GL066734>
- Sakamaki, K., Takahashi, E., Nakajima, Y., Nishihara, Y., Funakoshi, K., Suzuki, T., & Fukai, Y. (2009). Melting phase relation of FeH_x up to 20 GPa: Implication for the temperature of the Earth's core. *Physics of the Earth and Planetary Interiors*, 174(1–4), 192–201. <https://doi.org/10.1016/j.pepi.2008.05.017>
- Sata, N., Hirose, K., Shen, G., Nakajima, Y., Ohishi, Y., & Hirao, N. (2010). Compression of FeSi , Fe_3C , $\text{Fe}_{0.95}\text{O}$, and FeS under the core pressures and implication for light element in the Earth's core. *Journal of Geophysical Research*, 115(B9), B09204. <https://doi.org/10.1029/2009JB006975>
- Seto, Y., Nishio-Hamane, D., Nagai, T., & Sata, N. (2010). Development of a software suite on X-ray diffraction experiments. *The Review of High Pressure Science and Technology*, 20(3), 269–276. <https://doi.org/10.4131/jshpreview.20.269>
- Sha, X., & Cohen, R. E. (2010a). Elastic isotropy of ϵ -Fe under Earth's core conditions. *Geophysical Research Letters*, 37(10), L10302. <https://doi.org/10.1029/2009GL042224>
- Sha, X., & Cohen, R. E. (2010b). First-principles thermal equation of state and thermoelasticity of hcp Fe at high pressures. *Physical Review B*, 81(9), 094105. <https://doi.org/10.1103/PhysRevB.81.094105>
- Singh, A. K. (1993). The lattice strains in a specimen (cubic system) compressed nonhydrostatically in an opposed anvil device. *Journal of Applied Physics*, 73(9), 4278–4286. <https://doi.org/10.1063/1.352809>
- Singh, A. K., Balasingh, C., Mao, H.-k., Hemley, R. J., & Shu, J. (1998). Analysis of lattice strains measured under nonhydrostatic pressure. *Journal of Applied Physics*, 83(12), 7567–7575. <https://doi.org/10.1063/1.367872>
- Sumita, I., & Bergman, M. I. (2007). Inner-core dynamics. In P. Olsen (Ed.), *Treatise on geophysics, volume 8: Core dynamics* (pp. 299–318). Elsevier.
- Tateno, S., Hirose, K., Ohishi, Y., & Tatsumi, Y. (2010). The structure of iron in Earth's inner core. *Science*, 330(6002), 359–361. <https://doi.org/10.1126/science.1194662>
- Thomson, A. R., Nishihara, Y., Yamazaki, D., Tsujino, N., Hunt, S. A., Tsubokawa, Y., et al. (2023). Preliminary results from the New Deformation multi-anvil press at the Photon Factory: Insight into the creep strength of calcium silicate perovskite. In T. Nakagawa, M. Satish-Kumar, & T. Tsuchiya (Eds.), *Core-mantle coevolution: A multidisciplinary approach* (pp. 59–73). American Geophysical Union.
- Tsujino, N., Märza, A., & Yamazaki, D. (2020). Pressure dependence of Si diffusion in γ -Fe. *American Mineralogist*, 105(3), 319–324. <https://doi.org/10.2138/am-2020-7197>
- Tsujino, N., Yamazaki, D., Nishihara, Y., Yoshino, T., Higo, Y., & Tange, Y. (2022). Viscosity of bridgemanite determined by in situ stress and strain measurements in uniaxial deformation experiments. *Science Advances*, 8(13), eabm1821. <https://doi.org/10.1126/sciadv.abm1821>
- Uchida, T., Funamori, N., & Yagi, T. (1996). Lattice strains in crystals under uniaxial stress field. *Journal of Applied Physics*, 80(2), 739–746. <https://doi.org/10.1063/1.362920>
- Uchida, T., Wang, Y., Rivers, M. L., & Sutton, S. R. (2001). Stability field and thermal equation of state of ϵ -iron determined by synchrotron X-ray diffraction in a multianvil apparatus. *Journal of Geophysical Research*, 106(B10), 21799–21810. <https://doi.org/10.1029/2001JB000258>
- Van Orman, J. A. (2004). On the viscosity and creep mechanism of Earth's inner core. *Geophysical Research Letters*, 31(20), L20606. <https://doi.org/10.1029/2004GL021209>
- Wang, T., Song, X., & Xia, H. H. (2015). Equatorial anisotropy in the inner part of Earth's inner core from autocorrelation of earthquake coda. *Nature Geoscience*, 8(3), 224–227. <https://doi.org/10.1038/ngeo2354>
- Wenk, H.-R., Matthies, S., Hemley, R. J., Mao, H.-k., & Shu, J. (2000). The plastic deformation of iron at pressures of the Earth's inner core. *Nature*, 405(6790), 1044–1047. <https://doi.org/10.1038/35016558>
- Woodhouse, J. H., Giardini, D., & Li, X.-D. (1986). Evidence for inner core anisotropy from free oscillations. *Geophysical Research Letters*, 13(13), 1549–1552. <https://doi.org/10.1029/GL013i013p01549>
- Yamazaki, D., Ito, E., Yoshino, T., Yoneda, A., Guo, X., Zhang, B., et al. (2012). P-V-T equation of state for ϵ -iron up to 80 GPa and 1900 K using the Kawai-type high pressure apparatus equipped with sintered. *Geophysical Research Letters*, 39(20), L20308. <https://doi.org/10.1029/2012GL053540>
- Yamazaki, D., Tsujino, N., Yoneda, A., Ito, E., Yoshino, T., Tange, Y., & Higo, Y. (2017). Grain growth of ϵ -iron: Implications to grain size and its evolution in the Earth's inner core. *Earth and Planetary Science Letters*, 459, 238–243. <https://doi.org/10.1016/j.epsl.2016.11.049>
- Yoshida, S., Sumita, I., & Kumazawa, M. (1996). Growth model of the inner core coupled with outer core dynamics and the resulting elastic anisotropy. *Journal of Geophysical Research*, 101(B12), 28085–28103. <https://doi.org/10.1029/96JB02700>
- Yunker, M. L., & Van Orman, J. A. (2007). Interdiffusion of solid iron and nickel at high pressure. *Earth and Planetary Science Letters*, 254(1–2), 203–213. <https://doi.org/10.1016/j.epsl.2006.11.036>